Quantified contribution of β″ and β′ precipitates to the strengthening of an aged Al–Mg–Si alloy

Quantified contribution of β″ and β′ precipitates to the strengthening of an aged Al-Mg-Si alloy

Mingjun Yang[1], Haonan Chen[1], Andrey Orekhov[2], Qiang Lu[1], Xinyue Lan[1], Kai Li[1, 3, 4, *], Shuyan Zhang[4], Min Song[1, 3], Yi Kong[1], Dominique Schryvers[2], Yong Du[1, 3, 4, *]

[1]State Key Laboratory of Powder Metallurgy, Central South University, Changsha 410083, China

[2]Electron Microscopy for Materials Science (EMAT), Department of Physics, University of Antwerp, Antwerp, B-2020, Belgium

[3]Institute for Materials Microstructure, Central South University, Changsha 410083, China

[4]Centre of Excellence for Advanced Materials, Dongguan, Guangdong 523808, P.R. China

Abstract

It is generally believed that β″ precipitates, rather than β′ precipitates, are the major strengthening precipitates in aged Al-Mg-Si alloys. The reason for this difference is not well understood. To clarify this, two samples of the same Al-Mg-Si alloy but with different aging states were prepared. The under-aged sample only contains nano-precipitates of the β″ type, while the peak-aged one contains nearly equal volumes of β″ and β′ precipitates. We have, for the first time, separated the strengthening effect of the contribution from β″ and β′ precipitates, respectively, by an indirect approach based on high-precision measurements of volume fractions, number densities, sizes, proportions of the precipitates, their lattice strains, the composition and grain size of the matrix. The β′ precipitates, which take 45.6% of the total precipitate volume in the peak-aged sample, contribute to the entire precipitation strengthening by only 31.6%. The main reason why they are less useful compared to β″ precipitates has been found to be associated with their smaller lattice strains relative to the matrix,

1 which is 0.99% versus 2.10% (for β″).

2

3 **Key words:** TEM; yield strength; shear modulus; strain; mechanical model.

4 *Corresponding authors. Tel: + 86 18973163497 (KL); + 86 13974962527 (YD).

5 Email: leking@csu.edu.cn (KL); yong-du@csu.edu.cn (YD).

6

1. Introduction

With high strength-to-weight ratio, good formability and weldability, superior corrosion resistance, high electrical and thermal conductivity and attractive surface appearance, heat-treatable Al-Mg-Si-(Cu) alloys are widely used as body panels for the substitution of steel in the automotive industry to reduce the weight of vehicles and their energy consumption [1-3]. Generally, precipitation strengthening, solid solution strengthening and strain strengthening jointly determine the strength of Al-Mg-Si-(Cu) alloys, in addition to grain boundary strengthening which is less pronounced in 6xxx Al alloys as the grain size in this system is relatively stable during aging heat treatments [4-8]. The opinion that precipitation strengthening is the most important strengthening mechanism in Al-Mg-Si-(Cu) alloys has been widely accepted. The effect of precipitation strengthening mainly comes from the interaction between nanoscale precipitates and dislocations. For Al-Mg-Si alloys, the precipitation sequence is generally considered to be [9-12]:

super-saturated solid solution (SSSS) → atomic clusters → GP zones → β″→ β′, U1, U2, B′ → β, Si

In general, the needle-like β″ precipitate is considered to be the most efficient strengthening phase in 6xxx Al alloys.

Structures and compositions of the clusters and precipitates have been investigated in detail through several analytical methods including high-resolution transmission electron microscopy (HRTEM) [13, 14], electron diffraction [15], three-dimensional atom probe (3DAP) [16], high - angle annular dark field - scanning transmission electron microscopy (HAADF-STEM) [17], and energy-dispersive X-ray spectroscopy (EDX) [18]. Starting from the experimentally determined structures and compositions, the mechanical properties of the precipitates in Al-Mg-Si alloys have been predicted by Zhang et al. through first principles calculations [19]. Tab. 1 lists the crystal structure

parameters and elastic properties of the most common precipitates, i.e., needle-like β″ and β′ precipitates, in Al-Mg-Si alloys [13, 15, 19-21], in addition to those of the matrix phase Al [22-26]. Unfortunately, due to the size limitation of metastable β″ and β′ precipitates there is no experimental data for their mechanical parameters, specifically, for the shear modulus *G*, bulk modulus *B*, elastic modulus *E* and Poisson's ratio *v*.

Table 1

Related microstructure and elastic properties (bulk modulus-*B*, shear modulus-*G*, Young's modulus-*E* and Poisson's ratio-*v*) of β″, β′ phases and Al.

Phase	Shape	Composition	Space group	Lattice parameters/Å	*B*	*G*	*E*	*v*
β″	Needle	Mg_5Si_6	Monoclinic, C2/m	a = 15.16, b = 4.05, c = 6.74, β = 105.3° [15]	61.7 [19, 21]	34.2 [19, 21]	86.7 [19, 21]	0.27 [19, 21]
β′	Needle	Mg_9Si_5	Hexagonal, P63/m	a = 7.15, c = 12.15, γ = 120° [20]	56.9 [19]	37.4 [19]	92.0 [19]	0.23 [19]
Al	\	\	FCC, $Fm\bar{3}m$	a = 4.0494 [22]	75.2 [26]	26.5 [24]	70 [25]	0.345 [24]

Microstructural parameters of precipitates such as number density (n), volume fraction (V_f), size (average length l and average area of the cross-section A_{cs}) and types of the precipitates can drastically influence the magnitude of precipitation strengthening (σ_{ppt}). The higher the n value, the higher the probability of gliding dislocations impeded by precipitates, which leads to higher strength. Indeed, the length of precipitates will influence the intersections between precipitates and slip planes: the longer the precipitates, the higher the density of precipitates/slip-plan intersections, resulting in higher strength [27]. The larger the A_{cs}, the stronger the impediment to dislocation gliding during the deformation of the alloy. However, one should keep in mind the relationship $V_f = nlA_{cs}$ [28] and the fact that the solutes in an alloy that can be segregated to form precipitates increasing V_f is limited. The parameter A_{cs} also determines whether a precipitate is shearable or non-shearable [29], i.e., whether a gliding dislocation would shear or bypass a precipitate. The interaction mechanisms between

dislocations and precipitates in 6xxx Al alloys, especially for β″ and β′ precipitates, have been investigated by several authors [6, 30-34]. Dislocations were always found to shear β″ precipitates [30, 34] but bypass larger β′ precipitates [31, 32] during gliding. Moreover, Teichmann et al. [33] have reported that β′ precipitates with cross-section radii (r_{cs}) larger than 7.5 nm were bypassed by dislocations, while those with cross-section radii smaller than 7.5 nm were sheared by dislocations. In a yield strength model proposed by Esmaeili et al. [35], the relationship between average obstacle strength and average radius of precipitates at the peak-aged condition of an Al-Mg-Si alloy has been well analyzed, with consideration of the shearable to non-shearable transition. And some similar mechanical models proposed in recent years have also taken into account the influence of precipitates' microstructural parameters (n, l, r_{cs}, V_f, aspect ratio of precipitates and surface to surface distance between precipitates) and dislocation character on precipitation strengthening [35-45].

Furthermore, the mechanism of how precipitates strengthen Al-Mg-Si alloys has been intensively studied by experimental measurements and theoretical simulations [7, 29, 46-53]. It can be explained mainly from the following aspects: (i) difference in shear modulus between precipitates and the matrix leads to modulus strengthening (σ_{mod}), (ii) chemical strengthening (σ_{chem}), which results from the additional matrix-precipitate interface created by the dislocation when it shears through precipitates, and (iii) the lattice misfit between precipitates and the matrix produces an strain field around the coherent or semi-coherent precipitates, and results in coherency strengthening (σ_{coh}).

The coherent β″ precipitate was generally considered to have higher strengthening effect compared to the semi-coherent β′ precipitate [15, 54, 55], but such a statement is just qualitatively understood and remains veiled in the current stage.

The present work is aimed at quantifying the strengthening effect of both coherent β″ precipitates

and semi-coherent β′ precipitates by quantitative experimental characterization combined with strength modeling in a peak-aged Al-Mg-Si alloy. And the precipitation strengthening, modulus strengthening, chemical strengthening and coherency strengthening effects from both β″ and β′ precipitates are analyzed in detail.

2. Experimental and theoretical methods

2.1 Experimental

An Al-Mg-Si alloy was casted for this study and its chemical composition (wt.%) was determined as Al-0.66Mg-0.41Si by a photoelectric direct-reading spectrometer (Thermo ARL4460) . Fe was detected in the alloy at the impurity level of 0.11 wt.%. The as-cast alloy was homogenized at 500 °C for 12 h, hot and cold rolled to 1 mm thick sheets. Then the sheets were solution heat treated at 550 °C for 30 min, water-quenched to room temperature, and immediately aged at 180 °C for different times.

The Vickers microhardness of differently treated samples was tested on the mechanically polished surfaces with a load of 100 g and a dwell time of 15 s. Each of the presented values shown in Fig. S1 in the Supplementary Document averaged from ten measurements (excluding the maximum and minimum values). Tensile tests were conducted at room temperature using an Instron 3369 testing machine at a constant crosshead speed of 5 mm/min. The tensile samples with a gauge length of 25.0 mm and a width of 6.0 mm were cut from the 1.0 mm thick rolled sheets according to Ref. [56], and their long axes were parallel to the rolling direction. Each strength data point was the average value from two parallel samples tested.

TEM specimens were cut from the sheets and mechanically polished to the thickness of 50-80 μm, and then punched into disks with a diameter of 3 mm. The disks were thinned in an electrolyte with 33

vol.% Nitric acid in methanol using a Struers TenuPol-5 twin-jet electro-polishing instrument. TEM observations were performed using a FEI Tecnai G2 F20 S-Twin electron microscope operating at 200 kV. All images were taken along the $<001>_{Al}$ zone axis in order to characterize the cross-sections and side views of the needle/rod/lath precipitates. Geometric phase analysis (GPA) using a plugin script (written by Christoph T. Koch) installed in Gatan Digital-Micrograph Software was performed to map the lattice strain and lattice misfit [52, 55, 57-61]. And the lattice strain can be determined directly by measuring the lattice fringe shifts in HRTEM [62-64]. Generally, the level of lattice strains of precipitates is very low, which leads to a quite low signal to noise ratio [61]. In order to obtain a smooth lattice strain distribution in the matrix in the close vicinity of the precipitates, a digital process with a spatial resolution of 1.0 nm was used to smooth out the fluctuations resulting from imperfections in the images. The electro-polished disk with a diameter of 3 mm was also used for scanning electron microscope (SEM) observations in a FEI Helios Nanolab 650 instrument operating at 5 kV using electron channeling contrast imaging (ECCI) [65].

Samples aged for 3 h and 6 h were cut into thin bars of $0.5 \times 0.5 \times 20$ mm^3, and further thinned by standard two-step electro-polishing procedures to meet the requirements of 3DAP analysis [66]. The thin needle was tested in a LEAP 4000 HR instrument operating in voltage mode with a pulse fraction of 15% of DC voltage, under an ultrahigh vacuum better than 10^{-8} Pa, at a temperature of 50 K (-223°C), a pulse repetition rate of 200 kHz and a target evaporation rate of 0.5%. 3DAP data reconstruction, visualization and analysis were performed using the Imago Visualization and Analysis Software package (IVAS 3.6.12). Analysis of the precipitates present in each specimen was performed using isoconcentration surfaces (using Mg and Si at a minimum concentration of 5%) and the maximum separation algorithm within the IVAS software. More details can be found in Ref. [67]. The

separation distances (d_{max}) and minimum number of solutes (N_{min}) selected for the maximum separation algorithm were 0.7 nm and 10 solute atoms, respectively. These parameters were determined based on the methods described in Refs. [68, 69]. As N_{min} was set as 10, particles containing less than 10 detected solute atoms were not considered as precipitates. In addition, the detection efficiency of the 3DAP instrument is 36%.

2.2 Theoretical methods

According to the work of Esmaeili et al. [35], σ_{ppt} can be estimated by considering the cases of both non-shearable strong obstacles and shearable weak obstacles. It should be noted that the critical resolved shear stress was determined from the interaction of gliding dislocations with point obstacles, while the average obstacle spacing has been estimated by taking into account their shape and orientation relationship with the matrix [7, 35]. For strong obstacles, the equation is:

$$\sigma_{ppt} = \frac{MF_{peak}}{br_{peak}(2\pi)^{1/2}} V_f^{1/2} \qquad (1)$$

where M is the Taylor factor, b is the magnitude of the Burgers vector, V_f is the volume fraction of obstacles, r_{peak} and F_{peak} are the average radius of the equivalent circular cross-section and the average obstacle strength of the needle-like precipitates in peak-aged samples, respectively. For weak obstacles, the equation is:

$$\sigma_{ppt} = \frac{MF_{peak}^{3/2}}{b(2\sqrt{3}\pi)^{1/2}\Gamma^{1/2} r_{peak}^{3/2}} r^{1/2} V_f^{1/2} \qquad (2)$$

where $\Gamma = Gb^2/2$ is the dislocation line tension, $r = (3/2)^{1/4} r_{acs}$ is the radius of an average equivalent circular cross-section on slip plans $\{111\}_{Al}$ and r_{acs} is the average cross-section radius of precipitates. It should also be noted that the ratio between F_{peak} and r_{peak} can be considered as a constant in Al-Mg-Si alloys aged in the temperature range of 180 - 220 °C [35]:

$$\frac{F_{peak}}{r_{peak}} = \frac{F}{r} = \theta G b \quad (3)$$

where θ is the specific strength of the obstacle. In the following calculations, for distinguishing clearly σ_{ppt} under different conditions, $\sigma_{ppt\text{-}3h}$ and $\sigma_{ppt\text{-}6h}$ represent the contribution of precipitation strengthening to the yield strength of the samples aged for 3 h and 6 h, respectively. And $\sigma_{ppt\text{-}6h\text{-}\beta''}$ and $\sigma_{ppt\text{-}6h\text{-}\beta'}$ represent the contribution of precipitation strengthening to the yield strength of the sample aged for 6 h due to β″ and β′ precipitates, respectively.

In alloys where several strengthening mechanisms are operative at room temperature, resembling the mixture of a few strong and many weak obstacles, it is reasonable to assume that the individual strength contributions can be added linearly. Thus, the contribution of precipitation strengthening to the yield strength can be calculated by the following equation [7, 35-37, 70, 71]:

$$\sigma_y = \sigma_{ppt} + \sigma_{ss} + \sigma_g \quad (4)$$

where the σ_y is the overall strength of the artificially aged alloy considering the precipitation strengthening, solid solution strengthening (σ_{ss}) and the grain size strengthing effect (σ_g).

Moreover, in age hardened Al alloys, solute elements such as Mg, Si and Cu give rise to considerable solid solution strengthening, and it is assumed that the contribution from each element is additive. Therefore, σ_{ss} can be expressed as [37]:

$$\sigma_{ss} = \sum_j k_j C_j^{2/3} \quad (5)$$

where C_j is the concentration of a specific alloying element in the solid solution and k_j is the corresponding scaling factor.

Furthermore, as the Al-Mg-Si alloys are generally used in polycrystalline states, the grain size effect was also considered. The dependence of initial yield strength on grain size is often expressed by the Hall–Petch relation [70, 71]:

$$\sigma_g = \sigma_i + k_y d^{-1/2} \quad (6)$$

where σ_i is the intrinsic strength of Al, and k_y is the Hall-Petch constant being about 0.326 MPa $m^{-1/2}$ at $d^{-1/2} < 1500$ $m^{-1/2}$ (i.e., $d > 0.44$ μm, with d the diameter of the grain) for Al-Mg-Si alloys [71].

3. Experimental Results

3.1 Mechanical properties

According to the hardness curve in Fig. S1, the samples aged for 3 h (under-aged) and 6 h (peak-aged) were chosen for quantitative microstructural characterization. In addition, the engineering stress – strain curves were shown in Fig. S2. The yield strength of the samples aged for 3 h and 6 h were 258.6 ± 5.2 MPa and 273.3 ± 1.3 MPa (in the form of average value ± standard deviation), respectively.

3.2 Quantification of precipitates in the sample aged at 180 ºC for 3 h

The length, cross-sectional area, number density and volume fraction of precipitates in the sample aged for 3 h have been measured with high precisions. Based on our previous work [28], the number density of precipitates is calculated by the following formula:

$$n = \frac{3N_v}{(l + 0.8t)A_{FOV}} \quad (7)$$

where N_v is the measured number of precipitates in a field of view (FOV) of the TEM sample, t is the thickness of the observed region and A_{FOV} is the area of the field of view.

The bright field image is shown in Fig. 1a, and from this image all the end-on needle-like precipitates (some examples are marked by red circles) along $[001]_{Al}$ with different cross-sectional geometries were counted. The value of N_v is 1463 ± 146 (measurement uncertainties in the form of standard deviation according to the evaluation in [28], in this paper all digits after the symbol ± mean

measurement uncertainties unless specified), and is the total number of the end-on needle-like precipitates in five bright field images, the other four images were obtained from the area adjacent to the area in Fig. 1a. The length l (as marked by red rectangles) has also been measured in these same five images: 500 precipitates growing along $[100]_{Al}$ and $[010]_{Al}$ in total were measured and yield an average length of 26.4 ± 1.2 nm. The corresponding A_{FOV} is 2428034.5 ± 97121.38 nm^2 (uncertainties evaluated according to scale bar calibration of HRTEM images) [28]. In addition, the average area of cross-section of the precipitates has been measured in 60 HRTEM images like Fig. 1b, and the obtained value of A_{cs} is 28.7 ± 1.7 nm^2. On the other hand, it is found that all of these 60 randomly selected precipitates in the 60 HRTEM images are characterized as β″ precipitates through indexing of their Fast Fourier transform (FFT) patterns. Therefore, it is reasonable to speculate that there are no other types of precipitates in the samples aged for 3 h. The thickness of the field of view was measured by convergent beam electron diffraction (CBED) according to the method established previously [28], and more detail about this method can be found elsewhere [28, 72]. The thickness (t) of the specimen is calculated as 154.16 ± 4.62 nm according to the CBED pattern and its analysis as shown in Fig. S3 [28, 73]. Then the number density n can be calculated as n = (1.21 ± 0.13) × 10^{22} m^{-3} according to Eq. (7). And furthermore, the volume fraction $V_f = nlA_{cs}$ can be calculated as (0.92 ± 0.10) %. All these parameters have been listed in Tab. 2.

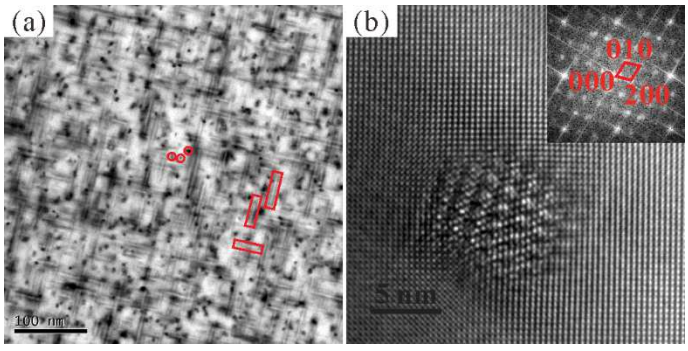

Fig. 1. TEM study of the sample aged at 180 ºC for 3 h. (a) bright field image, (b) HRTEM image

of a β″ precipitate with FFT pattern inserted. Z = $[001]_{Al}$.

Table 2

Summary of the parameters related to quantitative characterization of the precipitates in the Al-Mg-Si samples aged at 180 ºC for 3 h and 6 h, respectively. The digits after the symbol ± mean measurement uncertainties in the form of standard deviation.

Parameters	3 h	6 h ($N_{β″}$: $N_{β′}$ = 103 : 76)		
t (nm)	154.16 ± 4.62	129.73 ± 3.89		
A_{FOV} (nm^2)	2428034.45 ± 9712.38	2428034.45 ± 9712.38		
N_V	1463 ± 146	β″	β′	β″ + β′
		1570.9 ± 157	1159.1 ± 116	2730 ± 273
l (nm)	26.4 ± 1.2	26.2 ± 1.3	22.2 ± 3.5	24.5 ± 1.3
n (10^{22} m^{-3})	1.21 ± 0.13	1.51 ± 0.17	1.12 ± 0.12	2.63 ± 0.29
A_{CS} (nm^2)	28.7 ± 1.7	18.5 ± 1.1	20.7 ± 1.2	19.4 ± 1.2
r_{acs} (nm)	3.02 ± 0.09	2.43 ± 0.07	2.57 ± 0.08	2.49 ± 0.08
r	3.34 ± 0.10	2.69 ± 0.08	2.84 ± 0.09	2.76 ± 0.09
V_f (%)	0.92 ± 0.10	0.68 ± 0.08	0.57 ± 0.06	1.25 ± 0.14

Nomenclature: t - the thickness of the observed region, A_{FOV} - the area of the field of view, N_V - the measured number of precipitates in a field of view, l - the average length of precipitates, n - the number density of precipitates, A_{CS} – the average area of the end-on cross-section of precipitates, r_{acs} – the average cross-section radius of precipitates, r - the radius of an average equivalent circular cross-section on slip plans $\{111\}_{Al}$, V_f - the volume fraction of precipitates.

3.3 Quantification of precipitates in the sample aged for 6 h

For the peak-aged samples, i.e., samples aged for 6 h, a quantitative characterization was also performed and all the relative parameters have also been listed in Tab. 2. A typical bright field image is shown in Fig. 2a, and Figs. 2b-2d are HRTEM images of three kinds of classic precipitates in this sample. Through indexing the corresponding FFT patterns of 187 precipitates, it was concluded that 103 of these are β″ precipitates and 76 are β′ precipitates, the others being disordered precipitates. The percentage of disordered phases is thus so small that they can be ignored for the purpose of reducing the complexity and difficulty of quantitative microstructural analysis and modeling of the yield strength. It is necessary to mention that the length of β″ precipitates or β′ precipitates cannot be measured individually since these precipitates can only be recognized from their end-on cross-section. However,

the average l value of both β″ and β′ precipitates can be measured from a total of 500 precipitates growing along $[100]_{Al}$ and $[010]_{Al}$ in the bright field images (as marked by some red rectangles in Fig. 2a). As a result, the value of N_v is 2730 ± 273 and the average length of precipitates l = 24.5 ± 1.3 nm. The thickness of the field of view in this sample was calculated as 129.73 ± 3.89 nm from the CBED pattern as shown in Fig. S4. Finally, the number density and volume fraction of precipitates in the sample aged at 180 ºC for 6 h were measured as (2.63 ± 0.29) × 10^{22} m^{-3} and (1.25 ± 0.14) %, respectively.

Based on the soft-impingement theory [74, 75], the length of needle-shaped precipitates can be calculated by Eq. (8)

$$l = V_f^{1/3} - 8\sqrt{2}\frac{\gamma}{\Delta G_v} \quad (8)$$

Where ΔG_v is the free energy difference between matrix and precipitates per unit volume, and γ is the interface energy between precipitates and the matrix. At first, the average length ($l_{6h\text{-}\beta''}$) of β″ precipitates in the sample aged for 6 h can be calculated as 26.2 ± 1.3 nm based on the Eq. (8) and volume fraction of β″ precipitates in both samples aged for 3 h and 6 h. Then the average length of β′ precipitates can be calculated as 22.2 ± 3.5 nm based on the $l_{6h\text{-}\beta''}$ value and the number percentage between β″ and β′ precipitates in the sample aged for 6 h.

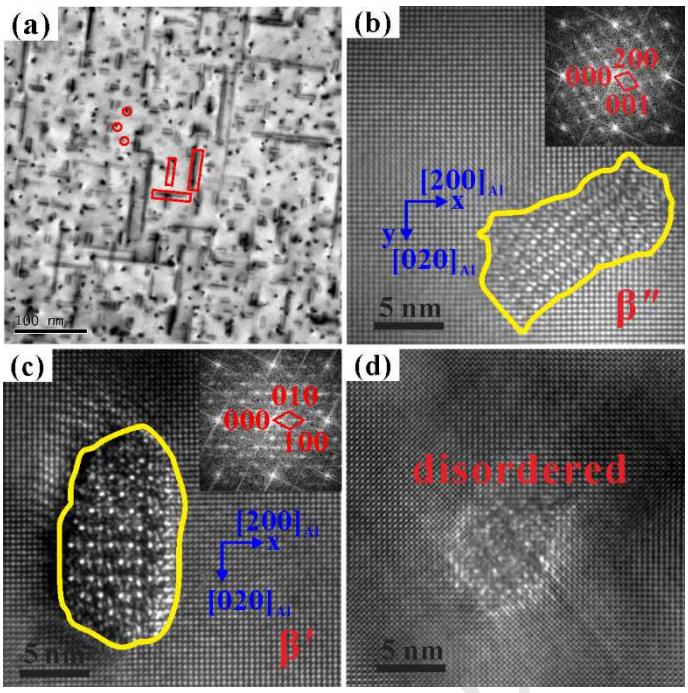

Fig. 2. TEM study of the sample aged at 180 ºC for 6 h. (a) bright field image, (b) and (c) HRTEM images of β″ and β′ precipitates with FFT patterns inserted, respectively. (d) HRTEM image of a disordered phase. Z = $[001]_{Al}$.

3.4 Determination of lattice strains of precipitates relative to the reference Al matrix

GPA has already been successfully applied to the analysis of strain distribution and lattice misfit of coherent or semi-coherent precipitates with a measurement standard deviation of about 0.1% - 0.2% [52, 53, 61, 63, 64, 76, 77]. This method is also applied here to deduce the lattice strains of both β″ and β′ precipitates relative to the reference Al matrix far away from the precipitate. For instance, $\varepsilon_{xx\text{-}\beta''}$ (shown in Fig. 3a) and $\varepsilon_{yy\text{-}\beta''}$ (shown in Fig. 3b) represent the lattice strain of the β″ precipitate relative to reference Al matrix (in Fig. 2b) along $[200]_{Al}$ and $[020]_{Al}$, respectively. The average value of $\varepsilon_{xx\text{-}\beta''}$ and $\varepsilon_{yy\text{-}\beta''}$ is taken as the net lattice strain of a given β″ precipitate. The average value $\varepsilon_{\beta''}$ from 12 β″ precipitates (excluding the maximum and minimum) equals to 2.10% ± 0.34% (in the form of average value ± standard deviation). It should be noted that the area marked within the yellow curve (the curve represent the manually distinguished interface between the precipitate and the matrix) is the target area for the GPA analysis. For instance, the average in-plane strain $\varepsilon_{xx\text{-}\beta''\text{-}1}$ and out-of-plane $\varepsilon_{yy\text{-}\beta''\text{-}1}$ determined

from the regions in the yellow curves in Figs. 3a-3b are 2.35% ± 0.07% and 1.71% ± 0.09% (average value ± standard deviation), respectively. Thus the $\varepsilon_{\beta''\text{-}1} = (|\varepsilon_{xx\text{-}\beta''\text{-}1}| + |\varepsilon_{yy\text{-}\beta''\text{-}1}|)/2$ = 2.03%. The value of $\varepsilon_{\beta''}$ is consistent with the results of 2% for GPA measurement and 3.5% for DFT & real-space analysis, more details can be seen in Ref. [52]. Similarly, as shown in the example of Figs. 3c-3d (GPA analysis of the β′ precipitate in Fig. 2c), 12 β′ precipitates were analyzed by GPA yielding a net $\varepsilon_{\beta'}$ of 0.99% ± 0.08% (average value ± standard deviation). In addition, the relationship between the lattice strains of these 2 × 12 individual β″ and β′ precipitates and their cross-sectional areas are shown in Fig. 4 in black solid squares and red solid circles, respectively.

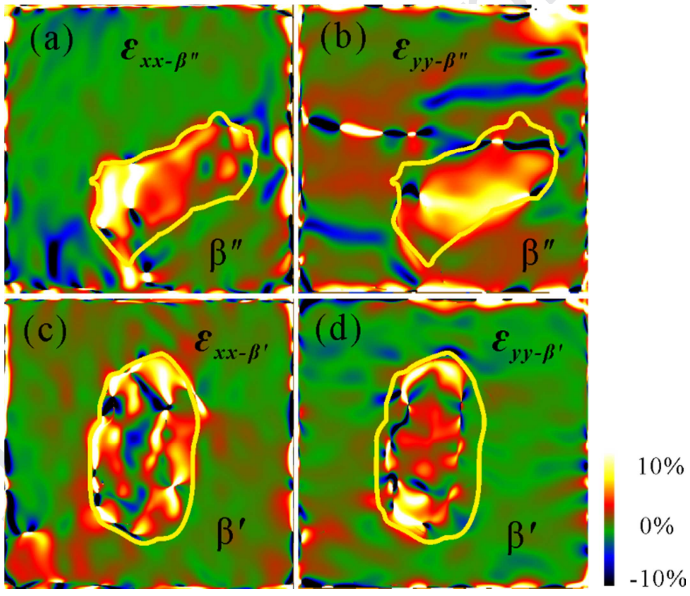

Fig. 3. GPA analysis for the lattice strains of the β″ and β′ precipitates relative to the Al matrix. Plot of the $\varepsilon_{xx\text{-}\beta''}$ (a) and $\varepsilon_{yy\text{-}\beta''}$ (b) component of β″ precipitate from Fig. 2b, $\varepsilon_{xx\text{-}\beta'}$ (c) and $\varepsilon_{yy\text{-}\beta'}$ (d) are the components of the β′ precipitate from Fig. 2c. x // $[200]_{Al}$, y // $[020]_{Al}$, z // $[002]_{Al}$. The areas marked in yellow curves correspond to the yellow curves marked in Figs. 2b-2c and which are used to analyze the lattice strains of the β″ and β′ precipitates, respectively.

Furthermore, the lattice strains of neither β″ precipitates nor β′ precipitates has shown any kind of numerical relationship with the precipitates' size. As shown in Fig. 4, it is easy to conclude that the lattice strains of β″ precipitates is concentrated in a range from 1.8% to 2.3%, while the range of lattice strains of β′ precipitates is from 0.8% to 1.2%.

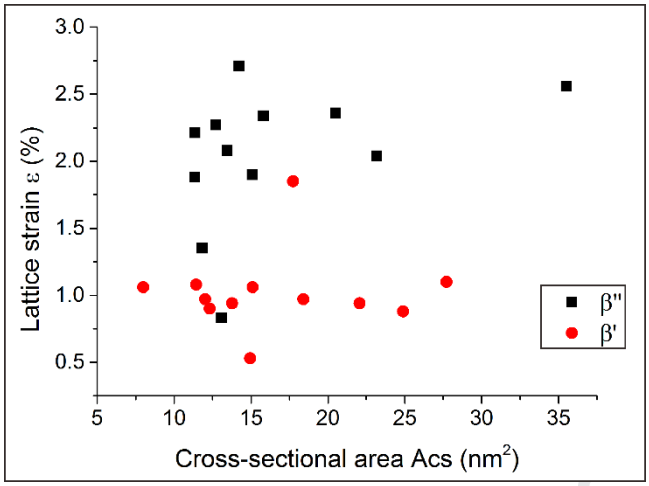

Fig. 4. Relationship between the lattice strains (ε) of the β″ and β′ precipitates and their cross-sectional area (A_{cs}) in the sample aged at 180 ºC for 6 h.

3.5 Determination of grain size and matrix composition

It is well known that grain refinement can synergistically improve strength and toughness of metals and alloys, including Al alloys [78-80]. For the Al-Mg-Si sheet samples that were cold-rolled in this work, the applied solution heat treatment at 550 °C for 30 min would lead to static recovery and recrystallization [81, 82]. In addition, Sepehrband et al. reported that the recrystallization would not be activated and the average grain diameter would not be changed in 6xxx alloys during artificial aging at temperatures below 235 °C [83]. Fig. 5 shows an electron channeling contrast image of the sample aged at 180 ºC for 6 h, which is used to calculate the grain size. The area of each of the 60 grains (S) was measured to obtain the equivalent grain diameter (D) through the formula $D = 2(S/\pi)^{1/2}$ under the assumption that the grains are spherical, and the average grain diameter d is calculated as 82.1 ± 13.6 μm (average value ± standard deviation).

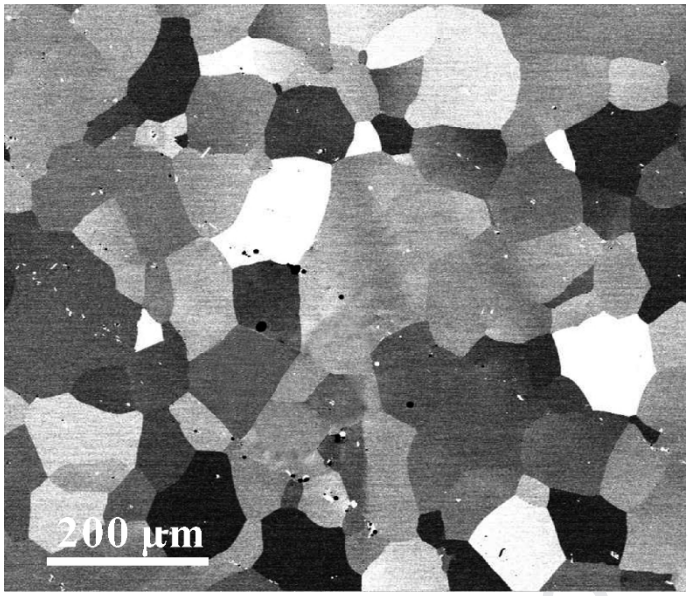

Fig. 5. Electron channeling contrast image of the sample aged at 180 ºC for 6 h and which was used to measure the grain size.

For the purpose of quantifying the contribution of solutes to the alloy strength, one can use the mass balance to back calculate the solute content of the matrix based on the quantified volume fractions of precipitates in the samples aged at 180 ºC for 3 h and 6 h, respectively. As a result, the matrix composition (wt.%) is determined as Al-0.39Mg-0.12Si and Al-0.22Mg-0.02Si for samples aged at 180 ºC for 3 h and 6 h, respectively. Furthermore, if the volume fraction of 0.29% of β-AlFeSi constituent should be considered in the back calculation, the matrix compositions were determined as Al-0.39Mg-0.08Si and Al-0.22Mg-(-0.02)Si (wt.%) for the samples aged for 3 h and 6h, respectively. It should be noticed that the volume fraction of β-AlFeSi was calculated by Thermo-Calc, as the non-uniform distribution of β-AlFeSi in the rolled and solid-solutionized sample makes measurement of its volume fraction difficult. The SEM and EDX results shown in Fig. S5 confirms the existence of β-AlFeSi in the solid-solutionized (as well as the aged) structure. Meanwhile, 3DAP analysis were conducted and the resultant elemental maps of Mg and Si in the samples aged at 180 ºC for 3 h and 6 h were shown in Figs. S6a and S6b, respectively. According to the results of 3DAP, the matrix composition (wt.%) is determined as Al-0.25Mg-0.18Si and Al-0.26Mg-0.08Si for samples aged at 180

ºC for 3 h and 6 h, respectively. Although the discrepancy between the matrix compositions determined by the mass balance method and by 3DAP is within 0.14 wt.% (and in this sense they mutually authenticate), such a discrepancy cannot be ignored. This may be caused by the many quantities needed to calculate matrix composition in the mass balance method, e.g. the alloy composition, the volume fractions and compositions of constituents, dispersoids and nanoprecipitates. For instance, the chemical composition of β′ precipitates has not yet been very accurately studied although a Mg_9Si_5 model was suggested according to electron diffraction and HRTEM [20], whether Si atom in β′ precipitates will be replaced by Al is still not clear. On the contrary, the fact that some Si atoms (in the Si_3 sites) are replaced by Al in the previously accepted β″-Mg_5Si_6 model has been unambiguously confirmed by Wenner et al. [18] using aberration-corrected STEM-EDX mapping at the low damage voltage of 80 kV. Therefore, the matrix composition determined by 3DAP is believed more precise in this case, and has been used in the following calculations.

4. Discussion

4.1 Separation of the contribution from different types of precipitates to the alloy strength

Due to that the volume fraction of β′ precipitates is about half of the total volume fraction of all precipitates in the sample aged for 6 h, it is necessary to analyze the contribution of β′ precipitates to the yield strength ($\sigma_{ppt\text{-}\beta'}$). According to Eqs. (1-6) and with input data shown in Tab. 3 [24, 37, 46, 48], the calculation process goes as follows:

Table 3

Summary of input data used in the present calculation of yield strength. The digits after the symbol ± denotes standard deviation from mean.

Parameters	Value	Comments
M	3.1	Magnitude of the Taylor factor [37]
b (m)	2.84×10^{-10}	Magnitude of the Burgers vector in

		Al [37]
G (N/m^2)	2.65×10^{10}	Magnitude of the shear modulus of Al [24]
σ_i (MPa)	10	Typical value for Pure Al [37]
k_{Si} (MPa/wt.%$^{2/3}$)	66.3	Scaling factor [37]
k_{Mg} (MPa/wt.%$^{2/3}$)	29.0	Scaling factor [37]
k_y	0.326	Hall-Petch coefficient [71]
$\gamma_{\beta''}$ (J/m^2)	0.084	Interfacial energy of β″/Al [46]
$\gamma_{\beta'}$ (J/m^2)	0.18	Interfacial energy of β′/Al [46]
$\varepsilon_{\beta''}$	2.10% ± 0.34%	Strain of β″ relative to Al matrix
$\varepsilon_{\beta'}$	0.99% ± 0.08%	Strain of β′ relative to Al matrix

Note: $\gamma_{\beta''}$ and $\gamma_{\beta'}$ were determined from an extended formulation of the 'nearest-neighbor broken-bond' model [46]. Therefore, $\gamma_{\beta''}$ and $\gamma_{\beta'}$ used in this work have no anisotropy.

a) For the sample aged at 180 ºC for 3 h

The tensile experiments yield $\sigma_{y\text{-}3h}$ = 258.6 MPa. Combining the results of 3DAP and Eq. (5), $\sigma_{ss\text{-}3h}$ = 32.6 MPa is found. By substituting d = 82.1 μm and σ_i = 10 MPa into the Eq. (6), the grain size effect $k_y d^{1/2}$ = 36.0 ± 1.3 MPa is found, and thus $\sigma_{ppt\text{-}3h} = \sigma_{y\text{-}3h} - \sigma_{ss\text{-}3h} - \sigma_i - k_y d^{1/2}$ = 180.0 ± 6.5 MPa. Then the ratio of F_{peak}/r_{peak} can be calculated as $4.85 \times 10^{-4} \pm 0.18 \times 10^{-4}$ N/m by combining Eqs. (2) and (3). It should be noted that both β″ and β′ precipitates (with radius much smaller than 7.5 nm) are considered as shearable in this work according to Refs. [30, 33, 34].

b) For the sample aged at 180 ºC for 6 h

Similarly, one can separate $\sigma_{y\text{-}6h}$ = 273.3 MPa into $\sigma_{ss\text{-}6h}$ = 24.1 MPa, σ_i = 10 MPa, $k_y d^{1/2}$ = 36.0 MPa and $\sigma_{ppt\text{-}6h}$ = 203.2 ± 2.6 MPa. As described above, the precipitation strengthening effect of the sample aged for 6 h comes from both β″ and β′ precipitates. According to Eq. (2), the contribution of β″ precipitates to the strengthening effect can be calculated as $\sigma_{ppt\text{-}6h\text{-}\beta''}$ = 138.9 ± 11.2 MPa. Thus for β' precipitates $\sigma_{ppt\text{-}6h\text{-}\beta'} = \sigma_{ppt\text{-}6h} - \sigma_{ppt\text{-}6h\text{-}\beta''}$ = 64.3 ± 11.5 MPa.

It is obvious that β″ precipitates have a higher strengthening effect compared to β′ precipitates, and this statement agrees well with the widely recognized conclusion that β″ precipitates are the main strengthening precipitates in Al-Mg-Si alloys [14, 54, 84, 85].

4.2 Reasons why β″ precipitates have higher strengthening effect compared with β′ precipitates

As mentioned in the *Introduction* section, modulus strengthening (σ_{mod}), chemical strengthening (σ_{chem}), coherency strengthening (σ_{coh}) jointly determine the strengthening effect of shearable precipitates [7, 51], and these three strengthening mechanisms can also be described by mathematical equations as follows:

$$\sigma_{ppt} = \sigma_{cut} = \sigma_{\mathrm{mod}} + \sigma_{ord} + \sigma_{coh} \tag{9}$$

$$\sigma_{\mathrm{mod}} = 0.0055M\left(\Delta G\right)^{3/2}\left(\frac{2V_f}{G}\right)^{1/2}\left(\frac{r}{b}\right)^{-1+3m/2} \tag{10}$$

$$\sigma_{\mathrm{chem}} = \left(\frac{6\gamma^3 bV_f}{\pi\Gamma}\right)^{1/2} r^{-1} \tag{11}$$

$$\sigma_{coh} = 2.6M\left(\left|\varepsilon\right|\right)^{3/2} G\left(\frac{2V_f r}{b}\right)^{1/2} \tag{12}$$

where ΔG is the difference of shear modulus between precipitates and the matrix, m is a constant which roughly equals 0.85 [7], lattice strain $\varepsilon = 2/3\delta$ and δ is the fractional misfit between the lattice parameters of precipitates and the matrix [7]. In addition, the interaction between precipitates and dislocations was simplified as the interaction between point obstacles and gliding dislocations as well [7]. And the aspect ratio of the precipitates (the half-length of the peripheral plane/the radius of the habit plane) was considered as a constant which will have an influence on the volume fraction of the precipitates. However, these assumptions will not affect this work as the radius of the habit plane and volume fraction were measured experimentally.

However, equation $\varepsilon = 2/3\delta$ cannot be used directly in Eq. (12) as which was proposed based on a spherical particle assumption. The lattice misfit increases during the transformation from coherent β″ precipitates to semi-coherent or incoherent post-β″ precipitates [86-88], and according to equation $\varepsilon = 2/3\delta$ and Eq. (12), the incoherent precipitate has a higher strengthening effect than that of

semi-coherent and coherent precipitates. This doesn't match with the actual fact that coherent precipitates have higher strengthening effect. In order to evaluate the strengthening effect of β′ and β precipitates in Al-Mg-Si alloys, Lang et al. [48] assumed that these precipitates nucleate on dislocations and the misfit between these precipitates and the matrix were taken as 0% in their work. Although this assumption does not agree well with our situation, the models based on this assumption provide a firm basis for modeling of the yield strength evolution of aged Al-Mg-Si alloys. However, such an assumption will lead to the lack of detailed insight into the strengthening effect of β′ or β precipitates.

In order to further confirm the fact that β″ precipitates have higher lattice strains than those of β′ precipitates, lattice fringes of Figs. 2b and 2c have been Fourier-filtered as shown in Figs. 6a-6b and Figs. 6c-6d, respectively. The misfit dislocations [53] at the precipitates/matrix interface have been marked in Fig. 6. And it's obviously that more dislocations can be found around the β″ precipitate than around the β′ precipitate as shown in Fig. 6. In order to maintain the coherency of precipitates with the matrix despite of the different lattice parameters, defects like misfit dislocations and vacancies will be produced [89-91]. And according to Hÿtch et al. [64], lattice strain will be produced due to defects like misfit dislocations. Therefore there is no doubt about the phenomena that β″ precipitates have higher lattice strains than β′ precipitates.

According to Vaithyanathan et al. [89], misfit strain, as one type of lattice strain, is irrelevant of the size of precipitates. At any rate, it is reasonable to take the lattice strains of both β″ and β′ precipitates as a constant (i.e., the average value of lattice strains of these precipitates) in the ensuing calculation. In a word, the present lattice strain cannot be estimated directly using equation $\varepsilon = 2/3\delta$ which maybe more suitable to estimate strains of spherical particles.

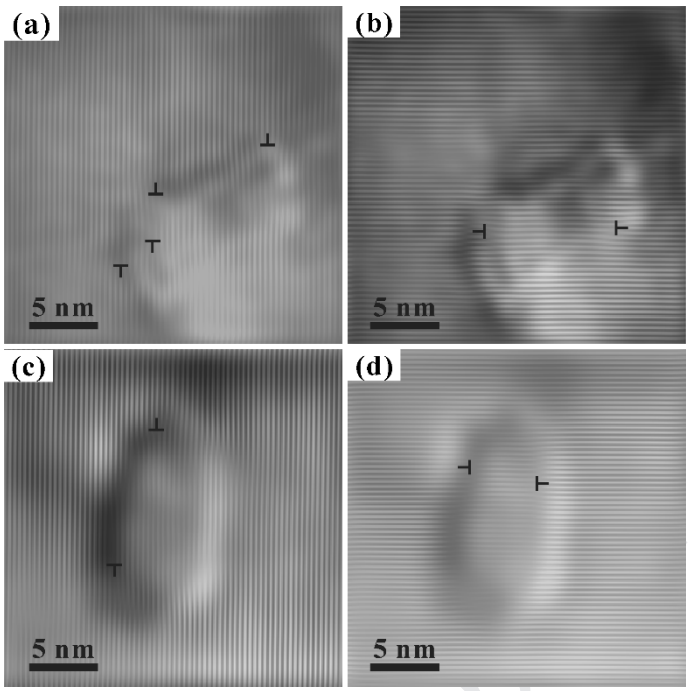

Fig. 6. Misfit dislocations at the precipitates/matrix interface. (a) and (b) are $(200)_{Al}$ and $(020)_{Al}$ lattice fringes obtained by filtering of Fig. 2b (for β″), respectively. (c) and (d) are $(200)_{Al}$ and $(020)_{Al}$ lattice fringes obtained by filtering of Fig. 2c (for β′), respectively. The edge dislocations were marked in the figures.

According to Eqs. (9-12) with related input data in Tabs. 1-3, the contribution of these three strengthening mechanisms to the yield strength can be calculated as follows:

a) For the sample aged for 3 h:

$$\sigma_{ppt-3h-1} = \sigma_{mod-3h} + \sigma_{chem-3h} + \sigma_{coh-3h} = 18.9 + 0.5 + 164.6 \text{ MPa} = 184.0 \text{ MPa} \quad (13)$$

b) For the contribution of β″ and β′ precipitates to the strength of the sample aged for 6 h:

$$\sigma_{ppt-6h-\beta''-1} = \sigma_{mod-6h-\beta''} + \sigma_{chem-6h-\beta''} + \sigma_{coh-6h-\beta''} = 15.3 + 0.5 + 127.0 \text{ MPa} = 142.8 \text{ MPa} \quad (14)$$

$$\sigma_{ppt-6h-\beta'-1} = \sigma_{mod-6h-\beta'} + \sigma_{chem-6h-\beta'} + \sigma_{coh-6h-\beta'} = 24.0 + 1.4 + 38.7 \text{ MPa} = 64.1 \text{ MPa} \quad (15)$$

$$\sigma_{ppt-6h-1} = \sigma_{ppt-6h-\beta''-1} + \sigma_{ppt-6h-\beta'-1} = 206.9 \text{ MPa} \quad (16)$$

From above calculation results, it is interesting to find that in the sample aged for 3 h the various strengthening effects, from strong to weak, are: coherency strengthening (164.6 MPa), modulus

strengthening (18.9 MPa) and chemical strengthening (0.5 MPa). This sequence is also apparent when one divides the contribution of β″ precipitates to the yield strength in the sample aged for 6 h. In addition, $\sigma_{ppt\text{-}3h\text{-}1}$ = 184.0, $\sigma_{ppt\text{-}6h\text{-}\beta''\text{-}1}$ = 142.8 MPa and $\sigma_{ppt\text{-}6h\text{-}1}$ = 206.9 MPa are very close to the above calculated results $\sigma_{ppt\text{-}3h\text{-}1}$ = 180.0 MPa, $\sigma_{ppt\text{-}6h\text{-}\beta''}$ = 138.9 MPa and $\sigma_{ppt\text{-}6h}$ = 203.2 MPa, respectively. The yield strengths calculated by mechanical models are consistent with experiments values. Fig. 7 shows the main calculation processes and results, and the key equations were also shown in it.

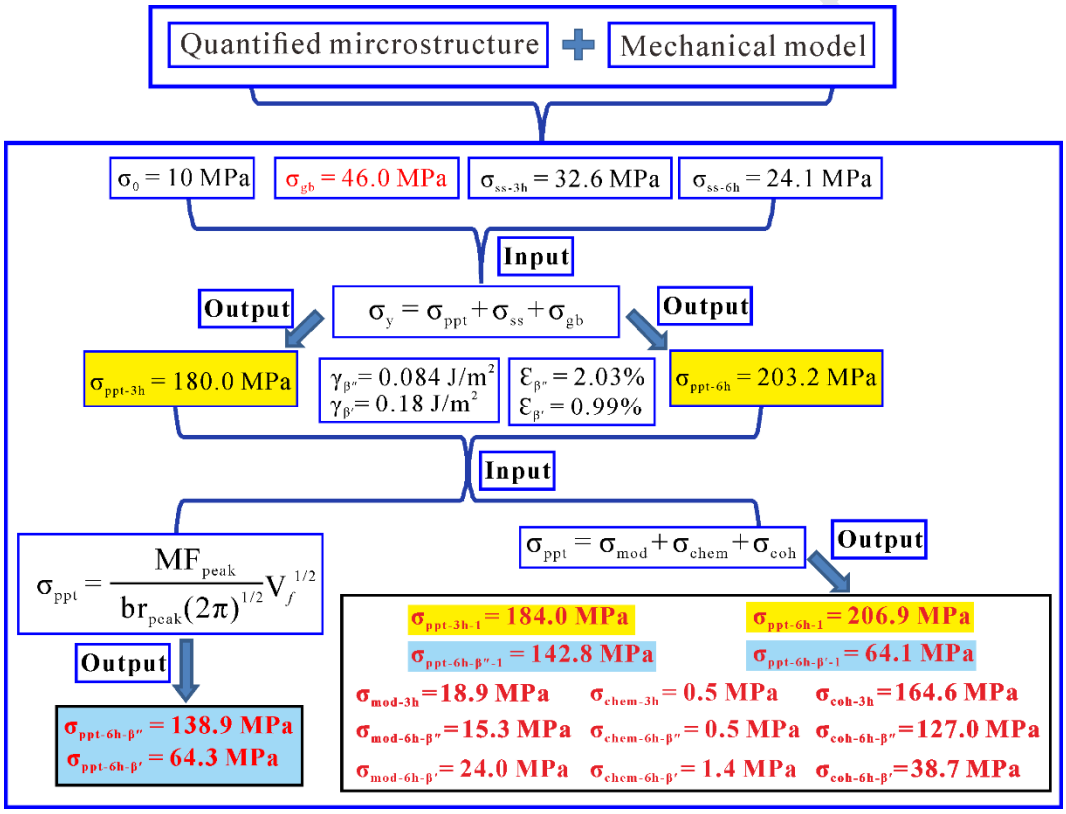

Fig. 7. Main calculation processes and results, and key equations.

4 Conclusions

By combining quantitative microstructural characterizations using SEM, TEM and 3DAP together with yield strength modeling, the strengthening mechanisms of both β″ and β′ precipitates have been studied in detail, and their contributions to the strengthening effect of an Al-Mg-Si alloy aged at 180 ºC for 3 h and 6 h were quantitatively analyzed. The findings are summarized as follows:

(1) After coarsening to a certain size, β″ precipitates start to dissolve and transform to β′ precipitates.

Therefore, in the peak-aged microstructure, β′ precipitates take a volume fraction of 0.57% ± 0.06% compared to that of 0.68% ± 0.08% for β″ precipitates.

(2) Lattice strain is one of the key factors which influences the coherency strengthening effect. The values of lattice strain of β″ and β′ precipitates relative to the matrix are determined as 2.10% ± 0.34% and 0.99% ± 0.08%, respectively, by GPA analysis. Furthermore, the precipitates' size does not appear to affect the lattice stains of both β″ and β′ precipitates relative to the matrix.

(3) The fractional lattice misfit was substituted by lattice stain of the precipitate relative to the matrix in the coherency strengthening model. The updated model has a higher adaptability and can be used to calculate the coherency strengthening effect of coherent and semi-coherent/incoherent precipitates. From this model, the coherency strengthening effect of β″ and β′ precipitates in the samples aged for 6 h can be determined as 127.0 MPa and 38.7 MPa, respectively. For β″ precipitates in the sample aged for 3 h this value reaches 164.6 MPa due to their higher volume fraction.

(4) The concept that β″ is the most efficient type of strengthening precipitate has been verified quantitatively for the first time. Under the peak-aged condition, β″ precipitates contribute 142.8 MPa to the yield strength of the alloy, while the value is 64.1 MPa for β′ precipitates. Obviously, the contribution of β′ precipitates to the yield strength is less, but still should not be ignored.

(5) At last, it is found that coherency strengthening, rather than modulus strengthening, is the main strengthening mechanism among the three strengthening mechanisms in the strengthening effect of coherent β″ precipitates, and the chemical strengthening effect can even be ignored. In contrast, both modulus strengthening and coherency strengthening contribute at similar levels to the

strengthening effect of semi-coherent β′ precipitates. In both cases, the contribution of chemical strengthening can be ignored.

Acknowledgement

This work was financially supported by National Natural Science Foundation of China (51531009, 51711530713, 51501230), Central South University (2018gczd033), the Flemish Science Foundation (FWO; VS.026.18N), and Program for Guangdong Introducing Innovative and Entrepreneurial Teams (2016ZT06G025) and Guangdong Natural Science Foundation (2017B030306014). The authors thank the Advanced Research Center of CSU for assistance in TEM experiments, as well as Prof. Dr. Lingfei Cao and Mr. Hui Song in Electron Microscopy Center of Chongqing University for performing 3DAP experiments.

Data Availability

The raw data required to reproduce these findings are available to download from [https://data.mendeley.com/datasets/xzybrc28jy/draft?a=a96f8662-6649-4207-999f-87e64497a172].

The processed data required to reproduce these findings are available to download from [https://data.mendeley.com/datasets/xzybrc28jy/draft?a=a96f8662-6649-4207-999f-87e64497a172].

References:

[1] W.S. Miller, L. Zhuang, J. Bottema, A.J. Wittebrood, P. De Smet, A. Haszler, A. Vieregge, Recent development in aluminium alloys for the automotive industry, Mater. Sci. Eng., A 280(1) (2000) 37-49.

[2] J. Hirsch, Aluminium in Innovative Light-Weight Car Design, Mater. Trans. 52(5) (2011) 818-824.

[3] J. Hirsch, Recent development in aluminium for automotive applications, Trans. Nonferrous Met. Soc. China 24(7) (2014) 1995-2002.

[4] H.R. Shercliff, M.F. Ashby, A process model for age hardening of aluminium alloys—I. The model, Acta Metall. Mater. 38(10) (1990) 1789-1802.

[5] D.H. Bratland, Ø. Grong, H. Shercliff, O.R. Myhr, S. Tjøtta, Overview No. 124 Modelling of precipitation reactions in industrial processing, Acta Mater. 45(1) (1997) 1-22.

[6] L.M. Cheng, W.J. Poole, J.D. Embury, D.J. Lloyd, The influence of precipitation on the work-hardening behavior of the aluminum alloys AA6111 and AA7030, Metall. Mater. Trans. A 34(11) (2003) 2473-2481.

[7] A.J. Ardell, Precipitation hardening, Metall. Trans. A 16(12) (1985) 2131-2165.

[8] G.B. Burger, A.K. Gupta, P.W. Jeffrey, D.J. Lloyd, Microstructural control of aluminum sheet used in automotive applications, Mater. Charact. 35(1) (1995) 23-39.

[9] T. Saito, C.D. Marioara, S.J. Andersen, W. Lefebvre, R. Holmestad, Aberration-corrected HAADF-STEM investigations of precipitate structures in Al–Mg–Si alloys with low Cu additions, Philos. Mag. 94(5) (2013) 520-531.

[10] A.G. Frøseth, R. Høier, P.M. Derlet, S.J. Andersen, C.D. Marioara, Bonding in MgSi and Al-Mg-Si compounds relevant to Al-Mg-Si alloys, Phys. Rev. B 67(22) (2003).

[11] M.A. van Huis, J.H. Chen, M.H.F. Sluiter, H.W. Zandbergen, Phase stability and structural features of matrix-embedded hardening precipitates in Al–Mg–Si alloys in the early stages of evolution, Acta Mater. 55(6) (2007) 2183-2199.

[12] M.A. van Huis, J.H. Chen, H.W. Zandbergen, M.H.F. Sluiter, Phase stability and structural relations of nanometer-sized, matrix-embedded precipitate phases in Al–Mg–Si alloys in the late stages of evolution, Acta Mater. 54(11) (2006) 2945-2955.

[13] S.J. Andersen, H.W. Zandbergen, J. Jansen, C. TrÆholt, U. Tundal, O. Reiso, The crystal structure of the β″ phase in Al–Mg–Si alloys, Acta Mater. 46(9) (1998) 3283-3298.

[14] S.J. Andersen, C.D. Marioara, R. Vissers, A. Frøseth, H.W. Zandbergen, The structural relation between precipitates in Al–Mg–Si alloys, the Al-matrix and diamond silicon, with emphasis on the trigonal phase U1-MgAl2Si2, Mater. Sci. Eng., A 444(1-2) (2007) 157-169.

[15] H.W. Zandbergen, S.J. Andersen, J. Jansen, Structure Determination of Mg_5Si_6 Particles in Al by Dynamic Electron Diffraction Studies, Science 277(5330) (1997) 1221.

[16] M. Murayama, K. Hono, M. Saga, M. Kikuchi, Atom probe studies on the early stages of precipitation in Al–Mg–Si alloys, Mater. Sci. Eng., A 250(1) (1998) 127-132.

[17] P.H. Ninive, A. Strandlie, S. Gulbrandsen-Dahl, W. Lefebvre, C.D. Marioara, S.J. Andersen, J. Friis, R. Holmestad, O.M. Løvvik, Detailed atomistic insight into the β″ phase in Al–Mg–Si alloys, Acta Mater. 69 (2014) 126-134.

[18] S. Wenner, L. Jones, C.D. Marioara, R. Holmestad, Atomic-resolution chemical mapping of ordered precipitates in Al alloys using energy-dispersive X-ray spectroscopy, Micron 96 (2017) 103-111.

[19] B. Zhang, L. Wu, B. Wan, J. Zhang, Z. Li, H. Gou, Structural evolution, mechanical properties,

and electronic structure of Al–Mg–Si compounds from first principles, J. Mater. Sci. 50(19) (2015) 6498-6509.
[20] R. Vissers, M.A. van Huis, J. Jansen, H.W. Zandbergen, C.D. Marioara, S.J. Andersen, The crystal structure of the β′ phase in Al–Mg–Si alloys, Acta Mater. 55(11) (2007) 3815-3823.
[21] R. Yu, J. Zhu, H.Q. Ye, Calculations of single-crystal elastic constants made simple, Comput. Phys. Commun. 181(3) (2010) 671-675.
[22] S. Popović, B. Gržeta, V. Ilakovac, R. Kroggel, G. Wendrock, H. Löffler, Lattice constant of the F.C.C. Al-rich α-Phase of Al-Zn alloys in equilibrium with GP zones and the β(Zn)-Phase, Phys. Status Solidi A 130(2) (1992) 273-292.
[23] H.F.S. Marcel, Y. Kawazoe, Prediction of solution enthalpies of substitutional impurities in aluminium, Modell. Simul. Mater. Sci. Eng. 8(3) (2000) 221.
[24] B. Bakó, E. Clouet, L.M. Dupuy, M. Blétry, Dislocation dynamics simulations with climb: kinetics of dislocation loop coarsening controlled by bulk diffusion, Philos. Mag. 91(23) (2011) 3173-3191.
[25] M.F. Ashby, Multi-objective optimization in material design and selection, Acta Mater. 48(1) (2000) 359-369.
[26] S. Raju, K. Sivasubramanian, E. Mohandas, The high temperature bulk modulus of aluminium: an assessment using experimental enthalpy and thermal expansion data, Solid State Commun. 122(12) (2002) 671-676.
[27] A. Bahrami, A. Miroux, J. Sietsma, An Age-Hardening Model for Al-Mg-Si Alloys Considering Needle-Shaped Precipitates, Metall. Mater. Trans. A 43(11) (2012) 4445-4453.
[28] K. Li, H. Idrissi, G. Sha, M. Song, J. Lu, H. Shi, W. Wang, S.P. Ringer, Y. Du, D. Schryvers, Quantitative measurement for the microstructural parameters of nano-precipitates in Al-Mg-Si-Cu alloys, Mater. Charact. 118 (2016) 352-362.
[29] T. Gladman, Precipitation hardening in metals, Mater. Sci. Technol. 15(1) (1999) 30-36.
[30] W.J. Poole *, X. Wang, D.J. Lloyd, J.D. Embury, The shearable–non-shearable transition in Al–Mg–Si–Cu precipitation hardening alloys: implications on the distribution of slip, work hardening and fracture, Philos. Mag. 85(26-27) (2005) 3113-3135.
[31] P. Donnadieu, G.F. Dirras, J. Douin, An Approach of Precipitate/Dislocation Interaction in Age-Hardened Al-Mg-Si Alloys: Measurement of the Strain Field around Precipitates and Related Simulation of the Dislocation Propagation, Mater. Sci. Forum 396-402 (2002) 1019-1024.
[32] K. Teichmann, C.D. Marioara, K.O. Pedersen, K. Marthinsen, The effect of simultaneous deformation and annealing on the precipitation behaviour and mechanical properties of an Al–Mg–Si alloy, Mater. Sci. Eng., A 565 (2013) 228-235.
[33] K. Teichmann, C.D. Marioara, S.J. Andersen, K. Marthinsen, TEM study of β′ precipitate interaction mechanisms with dislocations and β′ interfaces with the aluminium matrix in Al–Mg–Si alloys, Mater. Charact. 75 (2013) 1-7.
[34] K. Misumi, K. Kaneko, T. Nishiyama, T. Maeda, K. Yamada, K.-i. Ikeda, M. Kikuchi, K. Takata, M. Saga, K. Ushioda, Three-dimensional characterization of interaction between β″ precipitate and dislocation in Al–Mg–Si alloy, J. Alloy. Compd. 600 (2014) 29-33.
[35] S. Esmaeili, D.J. Lloyd, W.J. Poole, A yield strength model for the Al-Mg-Si-Cu alloy AA6111, Acta Mater. 51(8) (2003) 2243-2257.
[36] S. Esmaeili, D.J. Lloyd, W.J. Poole, Modeling of precipitation hardening for the naturally aged Al-Mg-Si-Cu alloy AA6111, Acta Mater. 51(12) (2003) 3467-3481.
[37] O.R. Myhr, Ø. Grong, S.J. Andersen, Modelling of the age hardening behaviour of Al–Mg–Si

alloys, Acta Mater. 49(1) (2001) 65-75.
[38] O.R. Myhr, Ø. Grong, H.G. Fjær, C.D. Marioara, Modelling of the microstructure and strength evolution in Al–Mg–Si alloys during multistage thermal processing, Acta Mater. 52(17) (2004) 4997-5008.
[39] E. Kozeschnik, J. Svoboda, P. Fratzl, F.D. Fischer, Modelling of kinetics in multi-component multi-phase systems with spherical precipitates, Mater. Sci. Eng., A 385(1-2) (2004) 157-165.
[40] G. Fribourg, Y. Bréchet, A. Deschamps, A. Simar, Microstructure-based modelling of isotropic and kinematic strain hardening in a precipitation-hardened aluminium alloy, Acta Mater. 59(9) (2011) 3621-3635.
[41] D. Bardel, M. Perez, D. Nelias, A. Deschamps, C.R. Hutchinson, D. Maisonnette, T. Chaise, J. Garnier, F. Bourlier, Coupled precipitation and yield strength modelling for non-isothermal treatments of a 6061 aluminium alloy, Acta Mater. 62 (2014) 129-140.
[42] C. Schäfer, O.R. Myhr, H.J. Brinkman, O. Engler, J. Hirsch, Modelling the Combined Effect of Room Temperature Storage and Cold Deformation on the Age-Hardening Behaviour of Al-Mg-Si Alloys-Part 2, Mater. Sci. Forum 794-796 (2014) 722-727.
[43] J.F. Nie, B.C. Muddle, Strengthening of an Al–Cu–Sn alloy by deformation-resistant precipitate plates, Acta Mater. 56(14) (2008) 3490-3501.
[44] J.F. Nie, B.C. Muddle, Comments on the “dislocation interaction with semicoherent precipitates (ω phase) in deformed Al-Cu-Mg-Ag alloy”, Scr. Mater. 42(4) (2000) 409-413.
[45] M.R. Ahmadi, B. Sonderegger, E. Povoden-Karadeniz, A. Falahati, E. Kozeschnik, Precipitate strengthening of non-spherical precipitates extended in 〈100〉 or {100} direction in fcc crystals, Mater. Sci. Eng., A 590 (2014) 262-266.
[46] Q. Du, K. Tang, C.D. Marioara, S.J. Andersen, B. Holmedal, R. Holmestad, Modeling over-ageing in Al-Mg-Si alloys by a multi-phase CALPHAD-coupled Kampmann-Wagner Numerical model, Acta Mater. 122 (2017) 178-186.
[47] V. Gerold, H. Haberkorn, On the Critical Resolved Shear Stress of Solid Solutions Containing Coherent Precipitates, Phys. Status Solidi B 16(2) (1966) 675-684.
[48] A.F. P. Lang, E. Povoden-Karadeniz, M.R. Ahmadi, P. Warczok, E. Kozeschnik, Modeling of the Yield Strength Evolution in Al-Mg-Si Alloys, Proceedings of 12th International Conference on Aluminium Alloys (ICAA-12) (2010) 1443-1448.
[49] M.R. Ahmadi, E. Povoden-Karadeniz, B. Sonderegger, K.I. Öksüz, A. Falahati, E. Kozeschnik, A model for coherency strengthening of large precipitates, Scr. Mater. 84-85 (2014) 47-50.
[50] M.R. Ahmadi, E. Povoden-Karadeniz, K.I. Öksüz, A. Falahati, E. Kozeschnik, A model for precipitation strengthening in multi-particle systems, Comput. Mater. Sci. 91 (2014) 173-186.
[51] M. Song, Modeling the hardness and yield strength evolutions of aluminum alloy with rod/needle-shaped precipitates, Mater. Sci. Eng., A 443(1-2) (2007) 172-177.
[52] L. Jones, S. Wenner, M. Nord, P.H. Ninive, O.M. Lovvik, R. Holmestad, P.D. Nellist, Optimising multi-frame ADF-STEM for high-precision atomic-resolution strain mapping, Ultramicroscopy 179 (2017) 57-62.
[53] L.L. Song, S. Liu, X. Mao, A new method for fast statistical measurement of interfacial misfit strain around nano-scale semi-coherent particles, RSC Adv. 7(45) (2017) 28506-28512.
[54] L. Ding, Z. Jia, J.-F. Nie, Y. Weng, L. Cao, H. Chen, X. Wu, Q. Liu, The structural and compositional evolution of precipitates in Al-Mg-Si-Cu alloy, Acta Mater. 145 (2018) 437-450.
[55] S. Wenner, R. Holmestad, Accurately measured precipitate–matrix misfit in an Al–Mg–Si alloy by

electron microscopy, Scr. Mater. 118 (2016) 5-8.
[56] Standard test methods for tension testing of metallic materials, ASTM E 8M-97 3 (1997) 77-97.
[57] M.J. Hÿtch, F. Houdellier, Mapping stress and strain in nanostructures by high-resolution transmission electron microscopy, Microelectron. Eng. 84(3) (2007) 460-463.
[58] Useful Plugins and Scripts for DigitalMicrograph, 2016. (Accessed Nov 14 2016).
[59] M. Hÿtch, E. Snoeck, R. Kilaas, Quantitative measurement of displacement and strain fields from HREM micrographs, Ultramicroscopy 74(3) (1998) 131-146.
[60] F.J.H. Ehlers, S. Dumoulin, Comment on "Accurately measured precipitate-matrix misfit in an Al Mg Si alloy by electron microscopy", Scr. Mater. 126 (2017) 69-70.
[61] J. Douin, P. Donnadieu, F. Houdellier, Elastic strain around needle-shaped particles embedded in Al matrix, Acta Mater. 58(17) (2010) 5782-5788.
[62] J. Chung, L. Rabenberg, Measurement of incomplete strain relaxation in a silicon heteroepitaxial film by geometrical phase analysis in the transmission electron microscope, Appl. Phys. Lett. 91(23) (2007) 231902.
[63] V.B. Özdöl, Characterization of strained semiconductor structures using transmission electron microscopy, Christian-Albrechts Universität Kiel, 2011.
[64] M.J. Hÿtch, J.-L. Putaux, J.-M. Pénisson, Measurement of the displacement field of dislocations to 0.03 Å by electron microscopy, Nature 423(6937) (2003) 270.
[65] S. Zaefferer, N.-N. Elhami, Theory and application of electron channelling contrast imaging under controlled diffraction conditions, Acta Mater. 75 (2014) 20-50.
[66] D.J. Larson, T.J. Prosa, R.M. Ulfig, B.P. Geiser, T.F. Kelly, Specimen Preparation, in: D.J. Larson, T.J. Prosa, R.M. Ulfig, B.P. Geiser, T.F. Kelly (Eds.), Local Electrode Atom Probe Tomography: A User's Guide, Springer New York, New York, NY, 2013, pp. 25-53.
[67] K. Buchanan, K. Colas, J. Ribis, A. Lopez, J. Garnier, Analysis of the metastable precipitates in peak-hardness aged Al-Mg-Si(-Cu) alloys with differing Si contents, Acta Mater. 132 (2017) 209-221.
[68] M.W. Zandbergen, Q. Xu, A. Cerezo, G.D.W. Smith, Study of precipitation in Al–Mg–Si alloys by Atom Probe Tomography I. Microstructural changes as a function of ageing temperature, Acta Mater. 101 (2015) 136-148.
[69] D. Vaumousse, A. Cerezo, P.J. Warren, A procedure for quantification of precipitate microstructures from three-dimensional atom probe data, Ultramicroscopy 95 (2003) 215-221.
[70] W.F. Hosford, Mechanical behavior of materials, Cambridge University Press2010.
[71] A. Loucif, R.B. Figueiredo, T. Baudin, F. Brisset, R. Chemam, T.G. Langdon, Ultrafine grains and the Hall–Petch relationship in an Al–Mg–Si alloy processed by high-pressure torsion, Mater. Sci. Eng., A 532 (2012) 139-145.
[72] D.B. Williams, C.B. Carter, Transmission Electron Microscopy: A Textbook for Materials Science, Springer US, Boston, MA, 2009.
[73] S.M. Allen, E.L. Hall, Foil thickness measurements from convergent-beam diffraction patterns An experimental assessment of errors, Philos. Mag. A 46(2) (1982) 243-253.
[74] F. Xu, X. Guo, P. Wu, J. Zhang, Y. Deng, Morphology Development and Kinetics of Plate or Rod Shaped Precipitates in Aluminum Alloys, Rare Metal Mat. Eng. 46(4) (2017) 876-881.
[75] J. da Costa Teixeira, D.G. Cram, L. Bourgeois, T.J. Bastow, A.J. Hill, C.R. Hutchinson, On the strengthening response of aluminum alloys containing shear-resistant plate-shaped precipitates, Acta Mater. 56(20) (2008) 6109-6122.
[76] W. Tirry, D. Schryvers, Linking a completely three-dimensional nanostrain to a structural

transformation eigenstrain, Nat. Mater. 8(9) (2009) 752-7.
[77] C.T. Koch, V.B. Özdöl, P.A. van Aken, An efficient, simple, and precise way to map strain with nanometer resolution in semiconductor devices, Appl. Phys. Lett. 96(9) (2010) 091901.
[78] B.S. Murty, S.A. Kori, M. Chakraborty, Grain refinement of aluminium and its alloys by heterogeneous nucleation and alloying, Int. Mater. Rev. 47(1) (2013) 3-29.
[79] G.M. Le, A. Godfrey, N. Hansen, W. Liu, G. Winther, X. Huang, Influence of grain size in the near-micrometre regime on the deformation microstructure in aluminium, Acta Mater. 61(19) (2013) 7072-7086.
[80] G. Sha, K. Tugcu, X.Z. Liao, P.W. Trimby, M.Y. Murashkin, R.Z. Valiev, S.P. Ringer, Strength, grain refinement and solute nanostructures of an Al–Mg–Si alloy (AA6060) processed by high-pressure torsion, Acta Mater. 63 (2014) 169-179.
[81] R. Garrett, J. Lin, T. Dean, An investigation of the effects of solution heat treatment on mechanical properties for AA 6xxx alloys: experimentation and modelling, Int. J. Plast 21(8) (2005) 1640-1657.
[82] F.J. Humphreys, M. Hatherly, Chapter 15 - Control of Recrystallization, in: F.J. Humphreys, M. Hatherly (Eds.), Recrystallization and Related Annealing Phenomena (Second Edition), Elsevier, Oxford, 2004, pp. 469-505.
[83] P. Sepehrband, X. Wang, H. Jin, S. Esmaeili, Microstructural evolution during non-isothermal annealing of a precipitation-hardenable aluminum alloy: Experiment and simulation, Acta Mater. 94 (2015) 111-123.
[84] Edwards GA, Stiller K, Dunlop GL, C. MJ, The precipitation Sequence in Al-MgSi Alloys, Acta Mater. 46(11) (1998) 3893-3904.
[85] S.J. Andersen, C.D. Marioara, A. Frøseth, R. Vissers, H.W. Zandbergen, Crystal structure of the orthorhombic U2-Al4Mg4Si4 precipitate in the Al–Mg–Si alloy system and its relation to the β′ and β″ phases, Mater. Sci. Eng., A 390(1-2) (2005) 127-138.
[86] W. Yang, L. Huang, R. Zhang, M. Wang, Z. Li, Y. Jia, R. Lei, X. Sheng, Electron microscopy studies of the age-hardening behaviors in 6005A alloy and microstructural characterizations of precipitates, J. Alloy. Compd. 514 (2012) 220-233.
[87] P. Dong, H. Li, D. Sun, W. Gong, J. Liu, Effects of welding speed on the microstructure and hardness in friction stir welding joints of 6005A-T6 aluminum alloy, Mater. Des. 45 (2013) 524-531.
[88] S. Dumolt, D. Laughlin, J. Williams, Formation of a modified β′ phase in aluminum alloy 6061, Scr. Metall. 18(12) (1984) 1347-1350.
[89] V. Vaithyanathan, C. Wolverton, L.Q. Chen, Multiscale modeling of θ′ precipitation in Al–Cu binary alloys, Acta Mater. 52(10) (2004) 2973-2987.
[90] R.G. Baker, D.G. Brandon, J. Nutting, The growth of precipitates, Philos. Mag. 4(48) (1959) 1339-1345.
[91] D.A. Smith, G. Shiflet, Low energy dislocation structures in interfaces, Mater. Sci. Eng. 86 (1987) 67-92.

Declaration of interests

☒ The authors declare that they have no known competing financial interests or personal relationships that could have appeared to influence the work reported in this paper.

☐The authors declare the following financial interests/personal relationships which may be considered as potential competing interests: